CHAPTER

FOURTEEN

TWO-DIMENSIONAL PHOTOELASTICITY

14.1 INTRODUCTION [1–5]

In a conventional two-dimensional photoelastic analysis a suitable model is fabricated, loaded, and placed in a polariscope, and the fringe pattern is examined and photographed. The next step in the photoelastic investigation is the interpretation of the fringe patterns, which in reality represent the raw test data. The purpose of this chapter is to discuss the interpretation of the isochromatic and isoclinic fringe patterns, compensation techniques, separation techniques, and scaling of the stresses between the model and prototype.

14.2 ISOCHROMATIC FRINGE PATTERNS [1–6]

The isochromatic fringe pattern obtained from a two-dimensional model gives lines along which the principal-stress difference $\sigma_1 - \sigma_2$ is equal to a constant. A typical example of a light-field isochromatic fringe pattern, which will be utilized to describe the analysis, is presented in Fig. 14.1. This photoelastic model represents a chain link subjected to tensile loads applied axially through roller pins. First, it is necessary to determine the fringe order at each point of interest on the model. In this example the assignment of the fringe order is relatively simple since seven rather obvious $\frac{1}{2}$-order fringes can quickly be identified. The two ovallike fringes located on the flanks of the teeth (labeled A) are of the $\frac{1}{2}$ order since the flank, because of its geometry, cannot support high stresses. The four fringes

Figure 14.1 Light-field isochromatic fringe pattern of a chain link subjected to axial tensile loads through the roller pins.

located at point B on the pinholes can be identified if the model is viewed with white light since zero-order fringes appear black while higher-order fringes are colored. Finally, the irregularly shaped fringe labeled C near the center of the link is of the $\frac{1}{2}$ order. Since the roller pins are located off the centerline of the plate, a combined state of tension and bending stresses is induced in the link plate with the neutral axis shifted to the right of the centerline of the plate.

With these $\frac{1}{2}$-order fringes established, it is a simple matter to determine the fringe order at any point in the model by progressively counting the fringes outward from the $\frac{1}{2}$-order location. For instance, the order of the fringe at the flank fillets is $7\frac{1}{2}$. When the fringe order at any point on the model has been established, it is possible to compute $\sigma_1 - \sigma_2$ from Eq. (13.8),

$$\sigma_1 - \sigma_2 = \frac{Nf_\sigma}{h}$$

where σ_1 and σ_2 are the principal stresses in the plane of the model. The maximum shear stress is given by

$$\tau_{\max} = \frac{1}{2}(\sigma_1 - \sigma_2) = \frac{Nf_\sigma}{2h} \tag{14.1}$$

provided σ_1 and σ_2 are of opposite sign and $\sigma_3 = 0$; otherwise

$$\tau_{max} = \begin{cases} \frac{1}{2}(\sigma_1 - \sigma_3) = \frac{1}{2}\sigma_1 & \text{if } \sigma_1 \text{ and } \sigma_2 \text{ are positive} \\ \frac{1}{2}(\sigma_3 - \sigma_2) = \frac{1}{2}\sigma_2 & \text{if } \sigma_1 \text{ and } \sigma_2 \text{ are negative} \end{cases} \tag{14.2}$$

The difference between Eq. (14.1) and Eqs. (14.2) is presented graphically in Fig. 14.2, where Mohr stress circles for two cases are given. When $\sigma_1 > 0$ and $\sigma_2 < \sigma_3 = 0$, the maximum shear stress is one-half the value of $\sigma_1 - \sigma_2$ and can be determined directly from the isochromatic fringe pattern according to Eq. (14.1). However, when $\sigma_1 > \sigma_2 > \sigma_3 = 0$, the maximum shear stress does not lie in the plane of the model, and Eq. (14.1) gives τ_p (see Fig. 14.2*b*) and not τ_{max}. To establish τ_{max} in this case it is necessary to determine σ_1 individually and not the difference $\sigma_1 - \sigma_2$. This is an important point since the maximum-shear theory of failure is often used in the design of machine components.

On the free boundary of the model, either σ_1 or σ_2 is equal to zero; hence, the stress tangential to the boundary can be determined directly from

$$\sigma_1, \sigma_2 = \frac{Nf_\sigma}{h} \tag{14.3}$$

The sign can usually be determined by inspection, particularly in the critical areas where the boundary stresses are a maximum. By referring to Fig. 14.1, it is apparent that the stresses in the flank fillets are tensile while the stresses along the back of the plate are compressive. On the free surface of the pinholes, the stresses

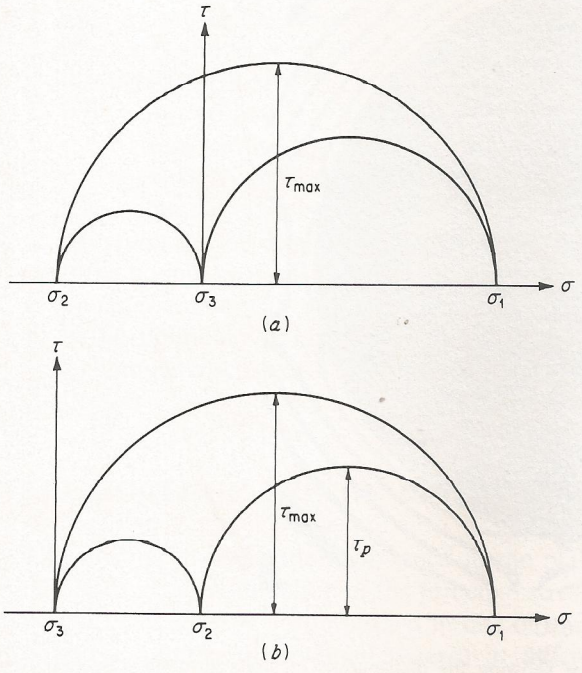

Figure 14.2 Mohr's circle for the state of stress at a point (*a*) $\sigma_1 > 0$, $\sigma_2 < \sigma_3 = 0$; (*b*) $\sigma_1 > \sigma_2 > \sigma_3 = 0$.

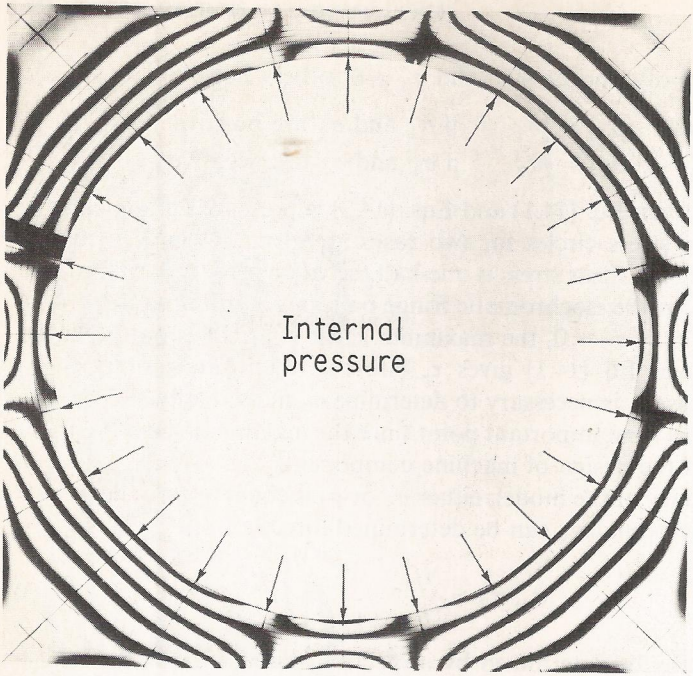

Light field

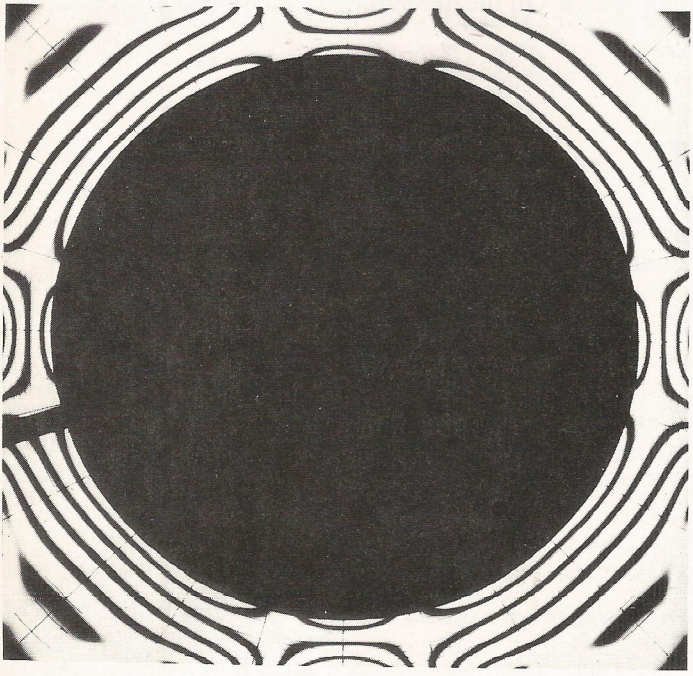

Dark field

Figure 14.3 Photoelastic fringe patterns showing the distribution of stress through a section of square tubing with a circular bore.

on the horizontal diameter are tensile and the stresses on the vertical diameter are compressive (see Sec. 3.14). The stresses on that portion of the boundary of the hole where the pin is in contact cannot be determined by applying Eq. (14.3) since the boundary is not free and, in general, σ_1 or σ_2 will not approach zero. In this case neither σ_1 nor σ_2 is known, a priori, and it is necessary to separate the stresses, i.e., individually determine the values of σ_1 and σ_2, at this region of contact on the pinhole. Methods to employ in separating the stresses are presented in Sec. 14.6.

As another example of the interpretation of isochromatic fringe patterns, consider the photograph presented in Fig. 14.3. In this instance a photoelastic model of square conduit with a circular borehole was analyzed. A uniformly distributed load was applied to the circular hole of the model. The stresses along the outside edges of the model can be determined directly from Eq. (14.3) since these edges represent free boundaries of the model. Along the boundary of the circular hole the surface is not free; however, in this case the stress σ_2 acting normal to the boundary is known to be equal to p, the applied load. Hence Eq. (13.8) becomes

$$\sigma_1 - \sigma_2 = \sigma_1 + p = \frac{Nf_\sigma}{h} \qquad \text{or} \qquad \sigma_1 = \frac{Nf_\sigma}{h} - p \tag{14.4}$$

where $\sigma_2 = -p$, since the applied pressure p is considered as a positive quantity.

In conclusion, it is clear that the isochromatic fringe pattern, once identified, can be interpreted in the following manner:

1. $\sigma_1 - \sigma_2$ can be determined at any point in the model from Eq. (13.8).
2. If $\sigma_1 > 0$ and $\sigma_2 < 0$, $\sigma_1 - \sigma_2$ can be related to the maximum-shear stress through Eq. (14.1).
3. If $\sigma_1 > \sigma_2 > 0$ or if $0 > \sigma_1 > \sigma_2$, $\sigma_1 - \sigma_2$ cannot be related to the maximum-shear stress and it is necessary to determine σ_1 and σ_2 individually and relate τ_{max} to σ_1 or σ_2 by Eq. (14.2).
4. If the boundary can be considered free (that is, σ_1 or $\sigma_2 = 0$), the other principal stress can be determined directly from Eq. (14.3).
5. If the boundary is not free but the applied normal load is known, the tangential boundary stress can be interpreted by applying Eqs. (14.4).
6. If the boundary is not free and the applied load is not known, separation techniques discussed in Sec. 14.6 must be applied to determine the boundary stresses.

14.3 ISOCLINIC FRINGE PATTERNS [1–6]

The isoclinic fringe pattern obtained in the plane polariscope is employed primarily to give the direction of the principal stresses at any point in the model. In practice this may be accomplished in one of two ways. The first procedure is to obtain a number of isoclinic patterns at different polariscope settings and to

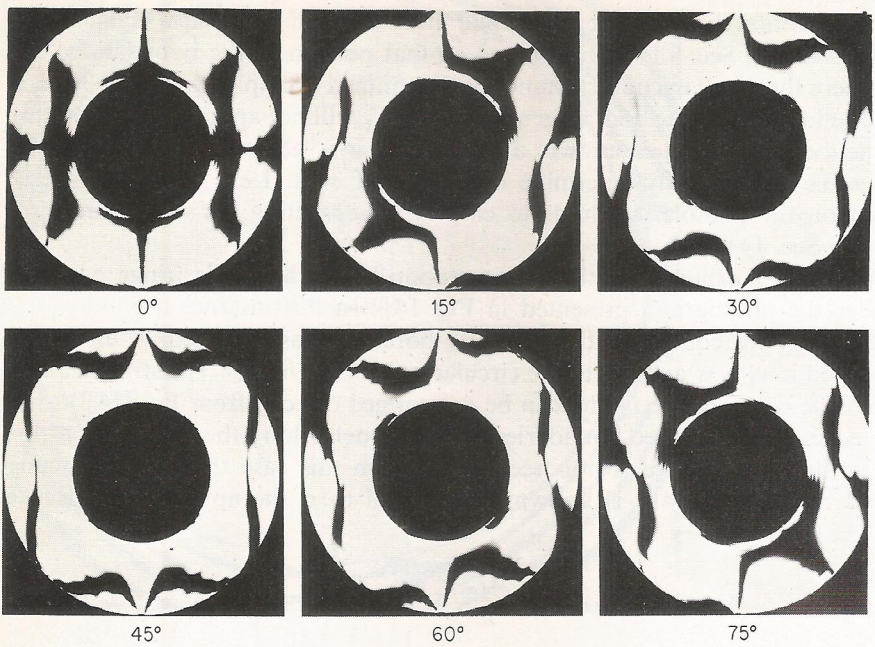

Figure 14.4 Isoclinic fringe patterns for a circular ring subjected to a diametral compressive load.

combine these fringe patterns to give one composite picture showing the isoclinic parameters over the entire field of the model. The second procedure is to isolate the points of interest and then to determine individually the polariscope setting, i.e., the isoclinic parameter, associated with each of these points.

An example of a series of isoclinic fringe patterns is shown in Fig. 14.4, where a thick-walled ring has been loaded in diametral compression. The data presented in this series of photographs are combined to give the composite isoclinic pattern illustrated in Fig. 14.5. Several rules can be followed in sketching the composite isoclinic patterns from the individual isoclinic fringe patterns. These rules are described below:

1. Isoclinics of all parameters must pass through isotropic or singular points.
2. An isoclinic of one parameter must coincide with an axis of symmetry in the model if an axis of symmetry exists.
3. The parameter of an isoclinic intersecting a free boundary is determined by the slope of the boundary at the point of intersection.
4. Isoclinics of all parameters pass through points of concentrated load.

An inspection of Figs. 14.4 and 14.5 will show that isoclinics of all parameters pass through the isotropic points as labeled by A through J. At isotropic points, $\sigma_1 = \sigma_2$ and all directions are principal; hence, isoclinics of all parameters must pass through these points. Again from an inspection of Fig. 14.5 it is clear that the

parameter of the isoclinic can be established by the slope of the boundary at its point of intersection. The reasoning for this behavior of isoclinics at free boundaries is based on the fact that the boundaries are isostatics or stress trajectories. That is, the tangential stress at the boundary is principal, and as such the isoclinic parameter must identify the slope of the boundary at the point of intersection. The axes of symmetry cannot support shear stresses; hence, these axes are principal directions and the isoclinics must identify them. The horizontal and vertical axes of the ring shown in Fig. 14.4 are axes of symmetry and are included in the 0° isoclinic family. Finally, at the points where a concentrated load is applied, the stress system in the local neighborhood of the load is principal in the r and θ directions, where the point of load application is the center of this local circle. It is clear then that the principal-stress directions will vary from 0 to 180° in this local region, and isoclinics of all parameters will converge at the point of load application, as illustrated in Fig. 14.5.

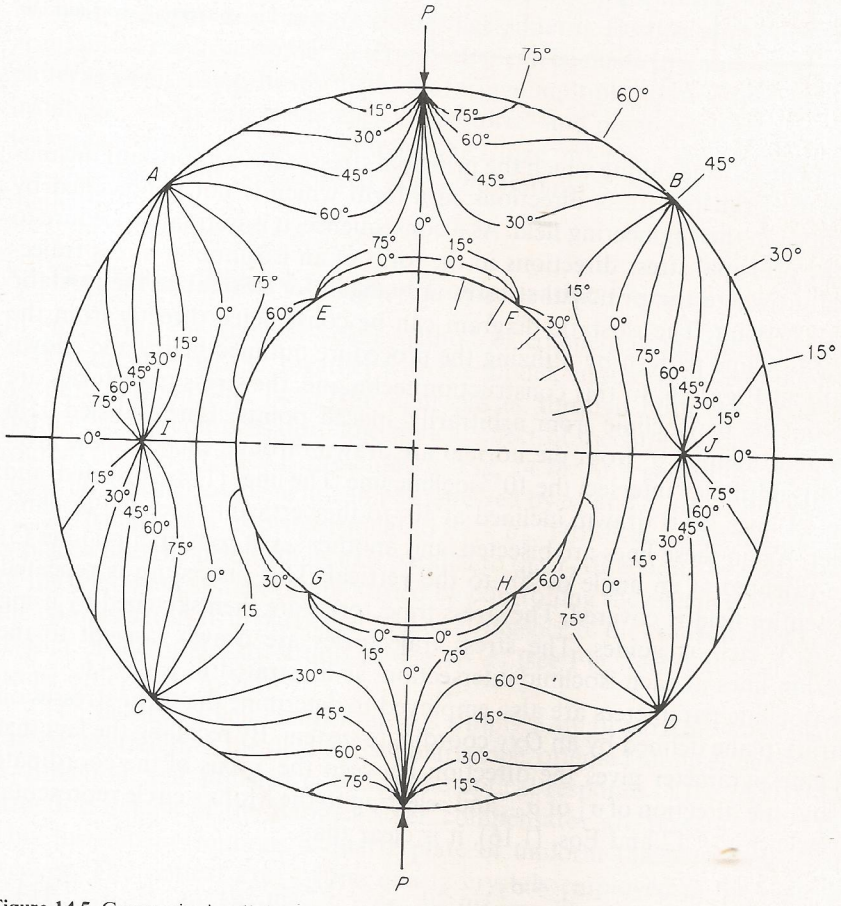

Figure 14.5 Composite isoclinic pattern for a circular ring subjected to a diametral compressive load.

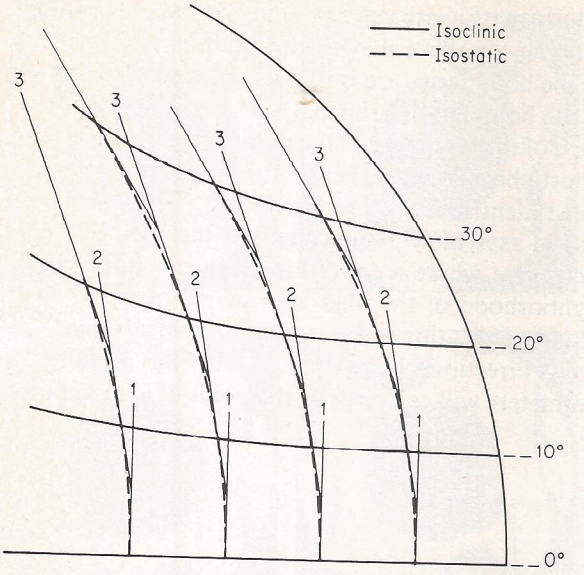

Figure 14.6 Construction technique for converting isoclinics to isostatics.

The isoclinics, lines along which the principal stresses have a constant inclination, give the principal-stress directions in a form which is not appreciated by other factions in the engineering field. As a consequence, it is normal procedure to present the principal-stress directions in the form of an isostatic or stress trajectory diagram where the principal stresses are tangent or normal to the isostatic lines at each point. The isostatic diagram can be constructed directly from the composite isoclinic pattern by utilizing the procedure outlined below and shown graphically in Fig. 14.6. In this construction technique, the stress trajectories are initiated on the 0° isoclinic from arbitrarily spaced points. Lines labeled 1 in Fig. 14.6 and oriented 0° from the normal are drawn through each of these arbitrary points until they intersect the 10° isoclinic line. The lines (1) are bisected, and a new set of lines (2) is drawn, inclined at 10° to the vertical to the next isoclinic parameter. Again these lines are bisected, and another set of construction lines (3) is drawn oriented at an angle of 20° to the vertical. This procedure is repeated until the entire field is covered. The stress trajectories are then sketched by using lines 1, 2, 3, etc., as guides. The stress trajectories are drawn tangent to the construction lines at each isoclinic intersection, as illustrated in Fig. 14.6.

The isoclinic parameters are also employed to determine the shear stresses on an arbitrary plane defined by an Oxy coordinate system. By recalling the fact that the isoclinic parameter gives the direction between the x axis of the coordinate system and the direction of σ_1 or σ_2, and referring to the Mohr's circle representation given in Fig. 1.12 and Eqs. (1.16), it is clear that

$$\tau_{xy} = -\frac{\sigma_1 - \sigma_2}{2} \sin 2\theta_2 = -\frac{Nf_\sigma}{2h} \sin 2\theta_2 \tag{14.5}$$

where θ_2 is the angle between the x axis and the direction of σ_2 as given by the isoclinic parameter. Also

$$\tau_{xy} = \frac{\sigma_1 - \sigma_2}{2} \sin 2\theta_1 = \frac{Nf_\sigma}{2h} \sin 2\theta_1 \tag{14.6}$$

where θ_1 is the angle between the x axis and the direction of σ_1 as given by the isoclinic parameter.

The combined isochromatic and isoclinic data represented in Eqs. (14.5) and (14.6) permit the determination of τ_{xy}. This value of τ_{xy} is used in the application of the shear-difference method (see Sec. 14.6A) for individually determining the values of σ_1 and σ_2.

14.4 COMPENSATION TECHNIQUES [7–13]

The isochromatic fringe order can be determined to the nearest $\frac{1}{2}$ order by employing both the light- and the dark-field fringe patterns. Further improvements on the accuracy of the fringe-order determination can be made by employing mixed-field patterns or by using Post's method of fringe multiplication. However, in certain instances even greater accuracies are required, and point-per-point compensation techniques are employed to establish the fringe order N. Two of these methods of compensation will be discussed here: the Babinet-Soleil method and the Tardy method.

A. The Babinet-Soleil Method of Compensation [7, 8]

In employing the Babinet-Soleil method of compensation, one inserts into the field of the polariscope, together with the model, another source of birefringence. As illustrated in Fig. 14.7*a*, the light passes through both the model and the Babinet-Soleil compensator. The optical effect of the superposition of these two sources of birefringence is presented in Fig. 14.7*b*. At a general point the state of stress on a principal element can be expressed by σ_1 and σ_2, and the optical effect, i.e., the fringe order, is proportional to $\sigma_1 - \sigma_2$. However, when the compensator is placed into the field with its axis parallel to the σ_2 direction, the optical response of the combined system can be varied by controlling the effective birefringence of the compensator. If, in particular, the birefringence of the compensator is set equal to that of the model by letting $\sigma^* = \sigma_1 - \sigma_2$ (see Fig. 14.7*b*), then the combined fringe order goes to zero.

The Babinet-Soleil compensator is simply a small variable wave plate which can be inserted into the field of the polariscope, oriented along either the σ_1 or the σ_2 direction, and adjusted to cancel the optical response of the model. The construction details of the Babinet-Soleil compensator are presented in Fig. 14.7*a*. This instrument contains a quartz plate of uniform thickness and two quartz wedges. The optical axes of the quartz crystals employed in the plate and the wedges are mutually orthogonal. Since quartz is a permanently doubly refracting

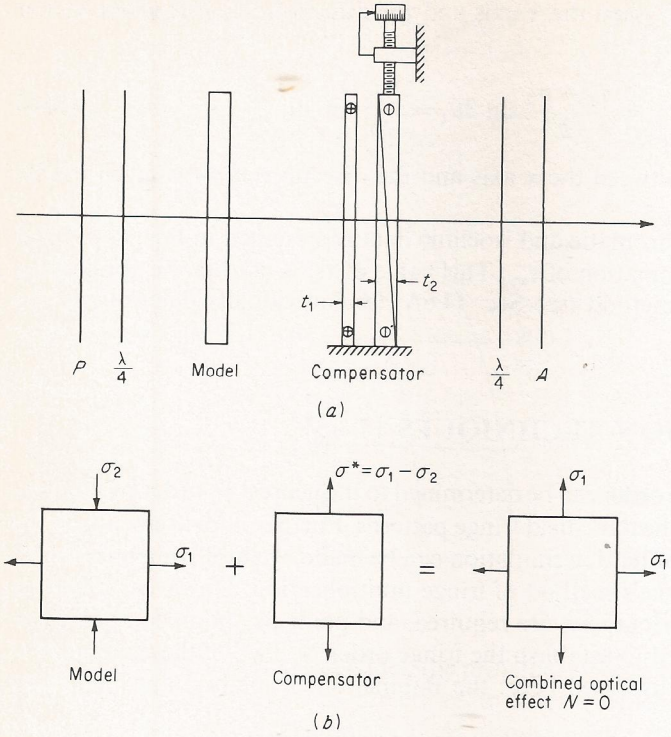

Figure 14.7 The Babinet-Soleil compensator: (*a*) light passing through the model and compensator; (*b*) superposition of retardation exhibited by model and compensator.

material, the birefringence exhibited by the compensator can be controlled by adjusting the thickness of the two wedges by turning a calibrated micrometer screw. The resultant retardation produced by this instrument depends upon the thickness of the quartz components t_1 and t_2. When $t_1 = t_2$, the retardation imposed is zero; however, for $t_2 \gtrless t_1$, both positive and negative retardation can be imposed on the system.

In practice, a point is selected on the model where the fringe order is to be determined precisely. Next, isoclinic parameters are established for this point to give the direction of either σ_1 or σ_2. The compensator is then aligned with the principal-stress direction and adjusted to cancel out the model retardation. The reading of the screw micrometer is proportional to the fringe order at the point in question. In this manner the determination of N can be made with at least two- and possibly three-decimal-point precision.

B. The Tardy Method of Compensation [9–13]

The Tardy method of compensation is very commonly employed to determine the order of the fringe at any arbitrary point on the model. Actually, the Tardy method is often preferred over the Babinet-Soleil method since no auxiliary equip-

ment is necessary and the analyzer of the polariscope serves as the compensating device. To employ the Tardy method, the polarizer of the polariscope is aligned with the principal direction of σ_1 at the point in question, and all other elements of the polariscope are rotated relative to the polarizer so that a standard dark-field polariscope exists. The analyzer is then rotated to produce extinction at the point. The interpretation of analyzer rotation in terms of fractional fringe order was discussed previously in Sec. 13.8.

14.5 CALIBRATION METHODS [1]

In most photoelastic analyses the stress distribution in a complex model is sought as a function of the load. To determine this stress distribution accurately requires the careful calibration of the material fringe value f_σ. Although the values of f_σ found in the technical literature are reasonably accurate, the material fringe values of photoelastic materials vary with the supplier, the batch of resin, temperature, and age. For this reason it is always necessary to calibrate each sheet of photoelastic material at the time of the test. Two methods are presented here which are recommended as both simple and accurate means of determining the material fringe value.

In any calibration technique one must select a body for which the theoretical stress distribution is accurately known. Preferably the model should also be easy to machine and simple to load. The calibration model is loaded in increments, and the fringe order and the loads are noted. From these data the material fringe value f_σ can be determined.

Consider first a tensile specimen having a width w and a thickness h, which is often employed as a calibration member. The axial stress induced in the necked region of the tensile specimen by the load P can be expressed as

$$\sigma_1 = \frac{P}{wh} \qquad \text{and} \qquad \sigma_2 = 0 \tag{14.7}$$

Substituting Eqs. (14.7) into Eq. (13.8) gives

$$\frac{P}{wh} = \frac{Nf_\sigma}{h} \qquad \text{or} \qquad f_\sigma = \frac{P}{wN} \tag{14.8}$$

This equation shows that the value of f_σ obtained from the tensile specimen is totally independent of its thickness h. In practice, a curve of the load P is plotted as a function of N (see Fig. 14.8) for five or six different points. The slope of the straight line drawn through these points is used for the value of P/N in Eqs. (14.8) to average out small errors in the reading of P and N.

The circular disk loaded in diametral compression is also employed as a calibration model. The circular disk is somewhat easier to machine and to load than the tensile specimen; moreover, if required, several calibration points can be obtained from a single load with this type of specimen.

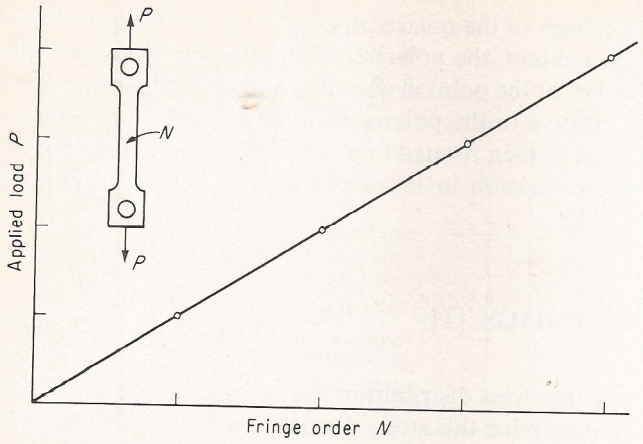

Figure 14.8 Typical calibration curve obtained by using a tensile specimen.

The stress distribution along the horizontal diameter (that is, $y = 0$) is given by

$$\sigma_{xx} = \sigma_1 = \frac{2P}{\pi hD}\left(\frac{D^2 - 4x^2}{D^2 + 4x^2}\right)^2$$

$$\sigma_{yy} = \sigma_2 = -\frac{2P}{\pi hD}\left[\frac{4D^4}{(D^2 + 4x^2)^2} - 1\right]$$

$$\tau_{xy} = 0 \tag{14.9}$$

where D = diameter of disk
x = distance along the horizontal diameter measured from center of disk
h = thickness of disk

The difference in the principal stresses $\sigma_1 - \sigma_2$ is

$$\sigma_1 - \sigma_2 = \frac{8P}{\pi hD}\frac{D^4 - 4D^2x^2}{(D^2 + 4x^2)^2} = \frac{Nf_\sigma}{h} \tag{14.10}$$

or

$$f_\sigma = \frac{8P}{\pi DN}\frac{D^4 - 4D^2x^2}{(D^2 + 4x^2)^2} \tag{14.11}$$

Equation (14.11) can be employed to calibrate photoelastic materials if a single load P is applied to the disk. In this case the fringe order N is determined as a function of x along the horizontal diameter. These values of N and x are then substituted into Eq. (14.11) to give several values of f_σ, which in turn are averaged to reduce errors in the reading of the fringe order.

More often, however, the center point of the disk, that is, $x = y = 0$, is used for the calibration point, and several values of load are applied to the model. In this instance, Eq. (14.11) reduces to

$$f_\sigma = \frac{8P}{\pi DN} \tag{14.12}$$

Again it is noted that the value of f_σ is independent of the model thickness h. The value of P/N substituted into this equation is determined by plotting several points of P versus N and establishing the slope of this straight line.

14.6 SEPARATION METHODS [1–5, 14–21]

In the analysis of isochromatic patterns, it was shown that the principal-stress difference $\sigma_1 - \sigma_2$ could be determined directly and that the maximum shear stress could be determined provided the two principal stresses are of opposite sign. Also, at free boundaries, the principal stress normal to the boundary is zero; therefore, the isochromatic data yield directly the value of the other principal stress. At interior regions of the model, individual values for the two principal stresses cannot be obtained directly from the isochromatic and isoclinic patterns without using supplementary data or employing numerical methods. The separation methods to be discussed here will be limited to those which are commonly used and will include methods based on: (1) the equilibrium equations, (2) the compatability equations, (3) Hooke's law, and (4) photoelasticity measurements at oblique incidence.

A. Methods Based on the Equilibrium Equations [1–5]

The two methods described in this section are based solely on the equations of equilibrium and as a result are independent of the elastic constants of the photoelastic model material. The first method, commonly referred to as the *shear-difference method*, is based on a graphical integration of the equations of equilibrium as expressed by Eqs. (1.3). The second method, commonly known as *Filon's method*, involves a graphical integration of a form of the equations of equilibrium known as the Lamé-Maxwell equations. Since both these methods are based on graphical integration techniques, they suffer from the limitation that errors are accumulated as the integration proceeds. Thus, extreme care must be exercised to ensure a high degree of accuracy in the original experimental data (isochromatics and isoclinics).

The shear-difference method [1, 2, 5] The equations of equilibrium (1.3) when applied to the plane-stress problem in the absence of body forces reduce to

$$\frac{\partial \sigma_x}{\partial x} + \frac{\partial \tau_{yx}}{\partial y} = 0 \qquad \frac{\partial \sigma_y}{\partial y} + \frac{\partial \tau_{xy}}{\partial x} = 0 \tag{14.13}$$

where σ_x, σ_y, and τ_{xy} are the normal and shear components of stress at an arbitrary point in the plane stress model under study. Solutions of the equilibrium equations can be obtained in the form

$$\sigma_x = (\sigma_x)_0 - \int \frac{\partial \tau_{yx}}{\partial y}\, dx \qquad \sigma_y = (\sigma_y)_0 - \int \frac{\partial \tau_{xy}}{\partial x}\, dy \tag{14.14}$$

which can be closely approximated by the finite-difference expressions

$$\sigma_x = (\sigma_x)_0 - \sum \frac{\Delta\tau_{yx}}{\Delta y}\Delta x \qquad \sigma_y = (\sigma_y)_0 - \sum \frac{\Delta\tau_{xy}}{\Delta x}\Delta y \tag{14.15}$$

In the above expressions, the terms $(\sigma_x)_0$ and $(\sigma_y)_0$ represent known stresses at points which have been selected as starting points for the integration process. Usually, these points are selected on free boundaries where the nonzero stress can be computed directly from the isochromatic data. The term τ_{xy} can be computed at any interior point of the model by using Eq. (14.6):

$$\tau_{xy} = \tfrac{1}{2}(\sigma_1 - \sigma_2) \sin 2\theta_1$$

When using this expression, care must be taken to maintain the proper algebraic sign for τ_{xy}. The expression as presented gives the sign of the shear stress in accordance with the theory-of-elasticity sign convention outlined in Chap. 1. The sign should be verified by inspection whenever possible. The term $\Delta\tau_{xy}$ is

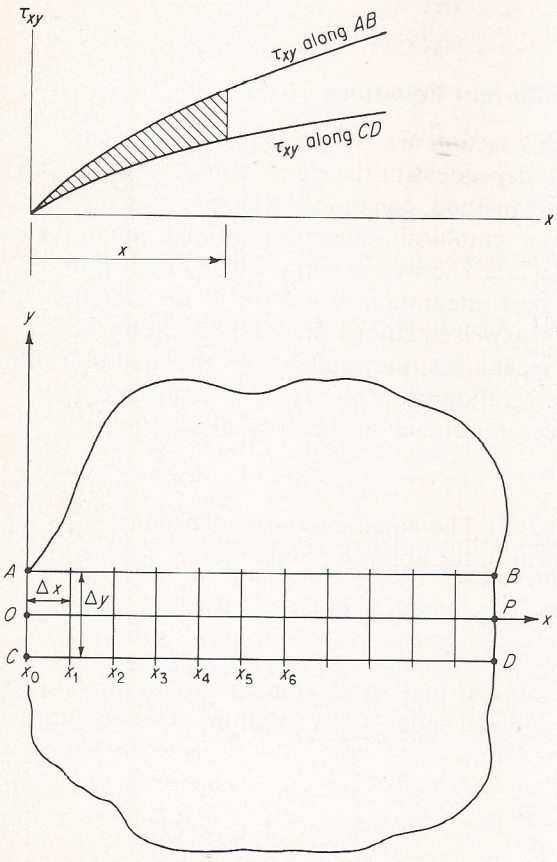

Figure 14.9 Grid system often employed in the application of the shear-difference method.

determined from a plot of the shear-stress distributions along two auxiliary lines (parallel to the line of interest and symmetrically located with respect to it), as illustrated in Fig. 14.9. From the figure it can be noted that the area (shown shaded) between the τ_{xy} curves represents the quantity $\sum \Delta\tau_{xy}\,\Delta x$. Thus, the accumulated area between the origin and a point at a distance x from the origin along the line of interest can be used to compute the difference between $(\sigma_x)_0$ and $(\sigma_x)_x$ simply by dividing by the distance Δy between the two auxiliary lines. Once σ_x is known at a given point, the value for σ_y can be computed from the expression

$$\sigma_y = \sigma_x - (\sigma_1 - \sigma_2)\cos 2\theta_1 \tag{14.16}$$

Equations (1.8), (1.9), and (13.8) can then be combined to give the two principal stresses as follows:

$$\sigma_1 = \frac{1}{2}(\sigma_x + \sigma_y) + \frac{1}{2}(\sigma_1 - \sigma_2) = \frac{1}{2}(\sigma_x + \sigma_y) + \frac{Nf_\sigma}{2h}$$

$$\sigma_2 = \frac{1}{2}(\sigma_x + \sigma_y) - \frac{1}{2}(\sigma_1 - \sigma_2) = \frac{1}{2}(\sigma_x + \sigma_y) - \frac{Nf_\sigma}{2h} \tag{14.17}$$

With the principal stresses and their orientation known at every point along the line, the state of stress is completely specified. The procedure can be repeated for any line of interest in the specimen.

Filon's method [1–4] Equilibrium of a small curvilinear rectangle bounded by four isostatics (stress trajectories) leads to a form of the equilibrium equations, commonly known as the Lamé-Maxwell equations, which can be expressed as

$$\frac{\partial\sigma_1}{\partial s_1} = -\frac{\sigma_1 - \sigma_2}{\rho_2} \qquad \frac{\partial\sigma_2}{\partial s_2} = -\frac{\sigma_1 - \sigma_2}{\rho_1} \tag{14.18}$$

where s_1 and s_2 are orthogonal curvilinear coordinates measured along the σ_1 and σ_2 isostatics, respectively, and ρ_1 and ρ_2 are the respective radii of curvature of these isostatics. When the isostatics are accurately known, this form of the equilibrium equations is easier to use than the cartesian form. Integrating along one of the isostatics yields

$$\sigma_1 = (\sigma_1)_0 - \int \frac{\sigma_1 - \sigma_2}{\rho_2}\,ds_1 \qquad \sigma_2 = (\sigma_2)_0 - \int \frac{\sigma_1 - \sigma_2}{\rho_1}\,ds_2 \tag{14.19}$$

Integration along an isostatic line can be performed by starting at a point of known stress, usually on a free boundary, and evaluating the integral from a plot of $(\sigma_1 - \sigma_2)/\rho_2$ versus s_1 or $(\sigma_1 - \sigma_2)/\rho_1$ versus s_2. The change in principal stress between the origin and the point of interest along the isostatic is the accumulated area under the curve. This method is certainly the most convenient when the problem of interest involves rotational symmetry. In this case, since the isostatics are concentric circles and radial lines, the isochromatics alone are sufficient for the integration. For an integration along a radial line, the radius of curvature needed for the integration is simply the distance from the axis of symmetry to the point

under consideration. The appropriate plot for evaluating the integral would be $(\sigma_1 - \sigma_2)/r$ versus r.

In the more general case of integration along an isostatic in an arbitrary stress field, the radius-of-curvature data are difficult to obtain with sufficient accuracy from photoelastic observations of the isoclinics. Brittle-coating isostatics can also provide the radii of curvatures, but this procedure is not recommended since more accurate methods are discussed in the subsections which follow.

B. Methods Based on the Compatibility Equations [14–17]

The compatibility or continuity equation for plane stress or plane strain in terms of cartesian stress components and with constant or zero body forces can be expressed in terms of the first invariant of stress as

$$\frac{\partial^2}{\partial x^2}(\sigma_{xx} + \sigma_{yy}) + \frac{\partial^2}{\partial y^2}(\sigma_{xx} + \sigma_{yy}) = 0 \tag{14.20}$$

Equations of this form are known as *Laplace's equation*, and any function which satisfies this equation is said to be a *harmonic function*. In photoelasticity, interest in Laplace's equation arises from the fact that the value of the function is uniquely determined at all interior points of a region if the boundary values are known. It was shown previously that the photoelastic isochromatics provide an accurate means for determining both the principal-stress difference $\sigma_1 - \sigma_2$ at all interior points of a two-dimensional model and, in many instances, complete boundary-stress information. Knowledge of the principal-stress sum $\sigma_1 + \sigma_2$ throughout the interior, together with the principal-stress difference $\sigma_1 - \sigma_2$ provides an effective means for evaluating the individual principal stresses.

Rigorous mathematical solution of Laplace's equation is possible only in cases where the boundary is relatively simple. Approximate solutions, which are sufficiently accurate for all practical work, can be obtained by numerical and experimental means. The Laplace equation serves as the governing equation in many other fields of engineering. Included are electrostatic fields in regions enclosed by boundaries at known potential, steady-state temperature distributions, and shapes of uniformly stretched films or membranes. Since the behavior of these different physical systems can be expressed in the same mathematical form, the one permitting the easier form of measurement can be used to study behavior in any of the other systems. These types of measurement methods are referred to as *analogy methods*.

In this section, three methods will be discussed for solving the Laplace equation. They include an analytic method, a numerical method, and an analogy method. The most important limitation of the methods described in this section is the requirement for complete knowledge of the boundary-stress distribution.

The analytic separation method [14] Solution of Laplace's equation by the method of separation of variables yields a sequence of harmonic functions which can be added together in a linear combination to give a series representation H of the first

Table 14.1 Solution of $\nabla^2 H = 0$ in various coordinate systems

	Coordinate system	Sequence of harmonic functions
Cartesian	$\dfrac{\partial^2 H}{\partial x^2} + \dfrac{\partial^2 H}{\partial y^2} = 0$	$1 \quad \sinh kx \sin ky \quad \sinh ky \sin kx$ $x \quad \sinh kx \cos ky \quad \sinh ky \cos kx$ $y \quad \cosh kx \sin ky \quad \cosh ky \sin kx$ $xy \quad \cosh kx \cos ky \quad \cosh ky \cos kx$
Polar	$\dfrac{\partial^2 H}{\partial r^2} + \dfrac{1}{r}\dfrac{\partial H}{\partial r} + \dfrac{1}{r^2}\dfrac{\partial^2 H}{\partial \theta^2} = 0$	$x = r\cos\theta \qquad y = r\sin\theta$ $1 \quad r^n \cos n\theta \quad r^n \sin n\theta$ $\ln r \quad r^{-n} \cos n\theta \quad r^{-n} \sin n\theta$
Bipolar	$\dfrac{\partial^2 H}{\partial \alpha^2} + \dfrac{\partial^2 H}{\partial \beta^2} = 0$	$x = \dfrac{C \sin\beta}{\cosh\alpha - \cos\beta} \qquad y = \dfrac{C \sinh\alpha}{\cosh\alpha - \cos\beta}$ $1 \quad \sinh n\alpha \sin n\beta \quad \cosh n\alpha \sin n\beta$ $\alpha \quad \sinh n\alpha \cos n\beta \quad \cosh n\alpha \cos n\beta$
Elliptic	$\dfrac{\partial^2 H}{\partial u^2} + \dfrac{\partial^2 H}{\partial^2 v} = 0$	$x = c\cosh u \cos v \qquad y = c\sinh u \sin v$ $1 \quad \sinh nu \sin nv \quad \cosh nu \sin nv$ $u \quad \sinh nu \cos nv \quad \cosh nu \cos nv$
Spherical	$\dfrac{\partial^2 H}{\partial r^2} + \dfrac{2}{r}\dfrac{\partial H}{\partial r} + \dfrac{1}{r^2}\dfrac{\partial^2 H}{\partial \phi^2} + \dfrac{1}{r^2 \tan\phi}\dfrac{\partial H}{\partial \phi} + \dfrac{1}{r^2 \sin^2\phi}\dfrac{\partial^2 H}{\partial \theta^2} = 0$	$x = r\sin\phi\cos\theta \qquad y = r\sin\phi\sin\theta \qquad z = r\cos\phi$ $r^m P_m^n \cos\phi \sin n\theta$ $r^{-m-1} P_m^n \cos\phi \sin n\theta$ where P is a Legendre function $r^m P_m^n \cos\phi \cos n\theta$ $r^{-m-1} P_m^n \cos\phi \cos n\theta$

stress invariant I. Solutions for H referred to several coordinate systems are presented in Table 14.1.

If the region of the model conforms to a regular coordinate system, determination of the proper coefficient for each function is considerably simplified. The sequence of functions when evaluated on the boundaries of the region reduces to a Fourier series. The unknown coefficients in these cases are the Fourier coefficients obtained by integrating the prescribed boundary values.

If the region of the model does not conform to a particular coordinate system, Fourier analysis cannot be employed to determine the coefficients which satisfy the prescribed boundary conditions. Instead, the method of least squares is used for the determination of the coefficients. A finite number of harmonic functions is first selected to appear in the series solution. Coefficients are then chosen such that the mean-square difference between the prescribed boundary values and the evaluation of the series along the boundary is minimized. If N harmonic functions F_1, $F_2, \ldots, F_N$ are selected and the associated unknown coefficients are denoted as C_1, $C_2, \ldots, C_N$, the series solution for the first stress invariant is

$$H = \sum_{n=1}^{N} C_n F_n \tag{14.21}$$

If $I(s)$ is used to represent the distribution of the first stress invariant along a boundary of total length L, H must be selected such that

$$\int_0^L \left[I(s) - \sum_{n=1}^{N} C_n F_n \right]^2 ds = \text{minimum} \tag{14.22}$$

The N unknown coefficients of this series can be evaluated by taking the partial derivative of the integral with respect to each of the coefficients and setting the resulting expressions equal to zero. Thus

$$\frac{\partial}{\partial C_k} \int_0^L \left[I(s) - \sum_{n=1}^{N} C_n F_n \right]^2 ds = 0 \qquad k = 1, 2, \ldots, N$$

which can be reduced to

$$\sum_{n=1}^{N} C_n \int_0^L F_n F_k \, ds = \int_0^L I(s) F_k \, ds \qquad k = 1, 2, \ldots, N \tag{14.23}$$

Equation (14.23) yields N simultaneous equations in terms of the N unknown coefficients. Solution of this set of equations gives the coefficients which provide the best match of boundary values possible with the initial selection of N harmonic functions. By increasing the number of functions in the series for H, the fit can be made as accurate as the original photoelastic determination of $I(s)$.

The four-point influence method [15] Numerical methods can be used very effectively to solve Laplace's equation. The method to be described here utilizes an iteration procedure by which estimated values of the harmonic function at points of interest of a network are systematically improved by making use of the fact that the value of the function at any point depends upon the values of the function at

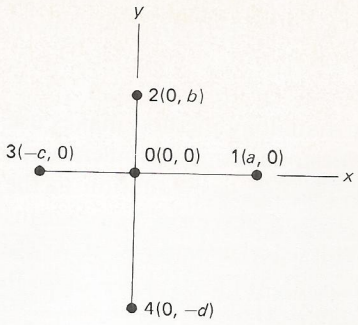

Figure 14.10 Network points in the general case.

neighborhood points. The basic relationship between values of the function at different points can be expressed by the four-point influence equation as

$$\Phi_0 = C_1\Phi_1 + C_2\Phi_2 + C_3\Phi_3 + C_4\Phi_4 \tag{14.24}$$

where neighborhood points in the most general case are located as shown in Fig. 14.10 and the constants C_1, C_2, C_3, and C_4 have the following values:

$$C_1 = \frac{bcd}{(bd + ac)(a + c)} \qquad C_2 = \frac{acd}{(bd + ac)(b + d)}$$

$$C_3 = \frac{abd}{(bd + ac)(c + a)} \qquad C_4 = \frac{abc}{(bd + ac)(d + b)} \tag{14.25}$$

In regions where a square array or network of points can be used, the computations are simplified since $C_1 = C_2 = C_3 = C_4 = \frac{1}{4}$.

Once the grid network has been established and the constants associated with each point evaluated, the known boundary values can be assigned to all points of intersection of the network with the boundary and estimated values or zero can be assigned to interior points. The value of each interior point is then improved by traversing the network in a definite sequence and using Eq. (14.24). Each time the network is traversed, the values are improved. The process is continued until the values become stationary or until further corrections do not alter the values more than a predetermined amount. At this stage in the procedure, further accuracy can be obtained only by using a finer-grid network.

In general, the labor involved in the process can be reduced by initially selecting a coarse network to establish reasonable values for the interior points. A fine network can then be introduced in selected regions (areas of high stress gradient) to improve the accuracy of the determinations in these regions.

The method suffers from the limitation that complete boundary-stress data must be available. Also, the method cannot be used to evaluate stress distributions along selected lines of interest without performing the evaluation for the complete model. Only symmetry considerations can be used to effect a reduction in the number of network points to be evaluated. The method has the advantage that isochromatic data alone are sufficient for the determinations. The method also has

the advantage that errors made during the iteration process have no influence on the final results. Errors simply increase the number of iterations required to obtain stationary values at interior points.

The electrical-analogy method [16, 17] The electrical-analogy method makes use of the fact that the voltage distribution in a uniformly conducting region enclosed by boundaries at known potential is governed by the Laplace equation in the same manner as the principal-stress sum in a plane-stress situation. Since means are readily available for applying and measuring voltage distributions, electrical measurements provide an excellent means for determining principal-stress sums in the interior of any complicated two-dimensional model.

An electrical model of the same geometry as the photoelastic model is prepared from a uniformly conducting material. Teledeltos paper, which consists of a uniform layer of graphite particles over a thin paper carrier, is a very suitable material from which to fabricate the electrical model. The Teledeltos paper, produced in widths up to 36 in (914 mm) and in lengths of several hundred feet (approximately 100 meters) is available with two different resistance values: 20 and 80 $k\Omega/in^2$ (30 and 120 $M\Omega/m^2$). Voltages applied to the boundary of the electrical model are proportional to the value of I_1 determined on the boundary of the photoelastic model. The values of I_1 on the boundary of the photoelastic model can be established from the isochromatic fringe pattern by using

$$I_1 = \sigma_1 + \sigma_2 = \sigma_1 - \sigma_2 = \frac{Nf_\sigma}{h} \tag{14.26}$$

since on a free boundary B either σ_1 or $\sigma_2 = 0$. The voltages applied to the boundary of the electrical model are of both a positive and a negative value, so that care should be exercised in applying the correct sign to the magnitude of the values obtained from Eq. (14.26). A typical circuit diagram illustrating the method

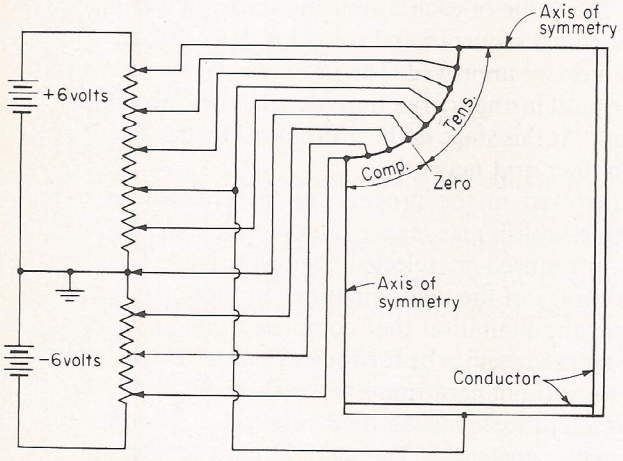

Figure 14.11 Electrical circuit for applying voltages to a Teledeltos paper model.

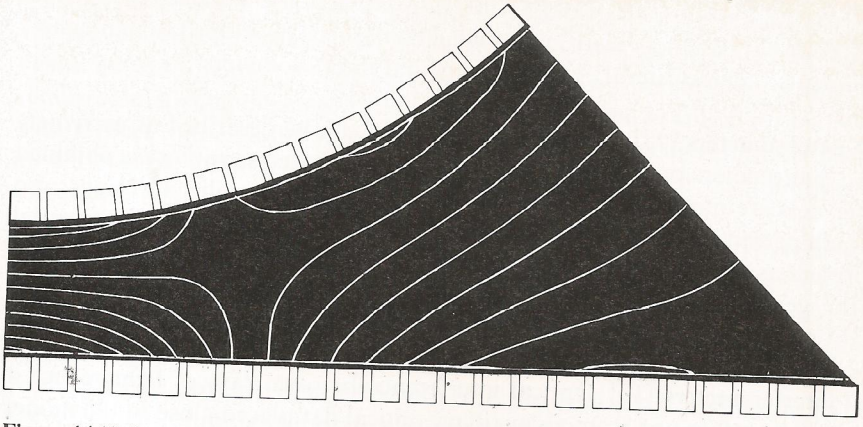

Figure 14.12 Isopachic pattern for a section of square tubing with a pressurized circular bore obtained using Teledeltos paper.

of applying voltages to the boundary of a Teledeltos paper model is illustrated in Fig. 14.11.† The graphite surface of the model is then probed with a high-impedance voltmeter to establish lines of constant voltage on the interior regions of the model. These lines of constant voltage are analogous to the isopachic lines where $\sigma_1 + \sigma_2 =$ constant. An example of the constant-voltage lines obtained for a section of square tubing with a pressurized circular bore is illustrated in Fig. 14.12. Isochromatic patterns for the same model were previously shown in Fig. 14.3.

The electrical-analogy method for separating principal stresses is one of the simplest, most rapid, and most accurate of the numerous techniques available. The equipment and skills required in applying the method are quite modest, and excellent results can quickly be achieved.

C. Methods Based on Hooke's Law [18, 19]

Separation methods based on Hooke's law make use of the fact that the strain in a direction perpendicular to the surface of a plane-stress model can be expressed as

$$\epsilon_{zz} = \frac{\Delta h}{h} = -\frac{\nu}{E}(\sigma_{xx} + \sigma_{yy}) = -\frac{\nu}{E}(\sigma_1 + \sigma_2)$$

or

$$\sigma_1 + \sigma_2 = -\frac{E}{\nu h}\Delta h \tag{14.27}$$

From Eq. (14.27) it is obvious that the sum of the principal stresses can be determined if the change in thickness of the model, as a result of the applied loads, can be measured accurately at the point of interest. The procedure requires a

† It should be noted here that this method can also be employed in heat transfer to solve the equation $\nabla^2 T = 0$. The constant-voltage lines in this case are analogous to isothermal lines.

device with high sensitivity since the thickness changes are seldom more than a few thousandths of an inch. Instruments which have been developed to make these measurements include lateral extensometers and interferometers.

Lateral extensometers [18] Lateral extensometers can be described as extremely sensitive micrometers or calipers. Quite often, the increased sensitivity is obtained by using delicate mechanical- or optical-lever systems. Specialized designs also exist which permit the use of electrical-resistance strain gages or linear differential transformers as the sensing elements. Extensometers are difficult to position and use if the geometry of the model is at all complicated. This method is recommended only for special situations where limited point data are desired.

Optical interferometers [19] Optical interference between rays of light reflected from a model surface and from an auxiliary optical flat placed close to the model surface provides an accurate means for determining the air gap between the two

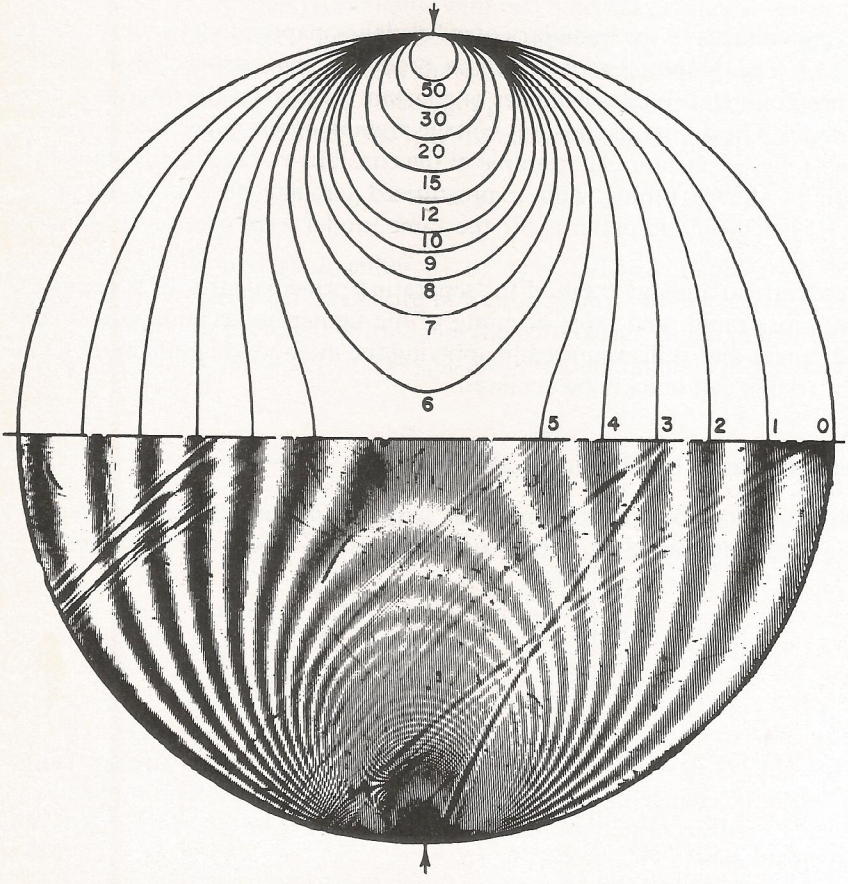

Figure 14.13 Isopachic fringe pattern obtained with a series interferometer. (*Courtesy of D. Post.*)

surfaces. Since the interference fringes which develop are loci of points of constant air-film thickness, they can be used to establish changes in model thickness and hence the sum of the principal stresses. Satisfactory application of this method requires an adequate means for locating and fixing the position of the optical flat with respect to the model and a model surface which is nearly optically flat so that an undesirable initial fringe pattern can be avoided. This second condition is often difficult to achieve.

Other interferometer systems which use transmitted rather than reflected light in their operation have been adapted for use in the determination of principal-stress sums. One such instrument, the series interferometer, was designed for this purpose and as a result is a simple and stable unit with a large-diameter field. The series interferometer and its operation were discussed in Sec. 11.7. A typical isopachic fringe pattern obtained with this instrument is shown in Fig. 14.13. Development of more elaborate systems, together with extensive use of the laser with its coherent and monochromatic light, has made optical interferometry a valuable experimental stress-analysis method for other applications.

D. Oblique-Incidence Methods [20, 21]

The equation developed for the stress optic law [Eq. (13.8)] was based on the light's passing through the model at normal incidence. However, if the model is rotated in the polariscope so that the light passes through the model at some other angle, an oblique-incidence fringe pattern can be observed. This oblique-incidence fringe pattern provides additional data which can be employed to separate the principal stresses.

Consider first the case where the principal stress directions are known and rotate the model about the σ_1 axis by an amount θ, as shown in Fig. 14.14. The light passes through the plane of the model obliquely and traverses a distance of $h/\cos\theta$ through the model. The fringe pattern produced is related to the secondary principal stresses lying in the plane normal to the axis of the light, which in

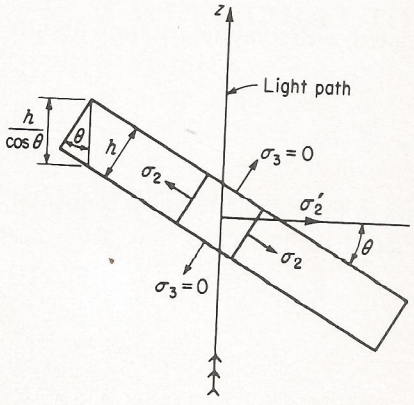

Figure 14.14 Rotation of the model about the σ_1 axis.

this case is the plane containing σ_1 and σ'_2. Thus

$$\sigma_1 - \sigma'_2 = \frac{f_\sigma N_\theta}{h/(\cos\theta)} \tag{14.28}$$

where N_θ is the fringe order associated with the oblique-incidence fringe pattern.

By applying Eqs. (1.16), it is clear that

$$\sigma'_2 = \sigma_2 \cos^2\theta$$

Hence

$$\sigma_1 - \sigma_2 \cos^2\theta = \frac{f_\sigma N_\theta}{h/(\cos\theta)} \tag{14.29}$$

By combining Eq. (14.29) (oblique incidence) with Eq. (13.8) (normal incidence), it can be shown that

$$\sigma_1 = \frac{f_\sigma}{h}\frac{\cos\theta}{\sin^2\theta}(N_\theta - N_0\cos\theta) \qquad \sigma_2 = \frac{f_\sigma}{h}\frac{1}{\sin^2\theta}(N_\theta\cos\theta - N_0) \tag{14.30}$$

where N_0 is the fringe order associated with the normal-incidence pattern.

By employing Eqs. (14.30) together with isochromatic fringe patterns from one normal- and one oblique-incidence photograph, it is possible to separate the principal stresses. This approach is often used to separate stresses along a line of symmetry where one rotation of the model about the line of symmetry provides sufficient data to separate the stresses along the entire length of the line.

Next consider the case where the principal-stress directions are not known and rotation of the model is made about arbitrary axes such as Oy and Ox.

In this instance three fringe patterns are obtained: the normal-incidence pattern, the oblique-incidence pattern corresponding to a rotation about Oy, and an oblique-incidence pattern corresponding to a rotation about Ox. The normal-incidence pattern gives, by Eqs. (13.8) and (1.12),

$$N_0 = \frac{h}{f_\sigma}(\sigma_1 - \sigma_2) = \frac{h}{f_\sigma}\sqrt{(\sigma_{xx} - \sigma_{yy})^2 + 4\tau_{xy}^2} \tag{a}$$

The oblique-incidence fringe pattern associated with a model rotation about Oy gives

$$N_{\theta y} = \frac{h}{\cos\theta_y}\frac{\sigma'_1 - \sigma'_2}{f_\sigma} \tag{b}$$

where σ'_1 and σ'_2 are secondary principal stresses in the $y'x'$ plane which is normal to the incident light along the z' axis. From Eqs. (1.12) it is clear that

$$\sigma'_1 - \sigma'_2 = \sqrt{(\sigma_{x'x'} - \sigma_{y'y'})^2 + 4\tau_{x'y'}^2} \tag{c}$$

and from Eqs. (1.6)

$$\sigma_{x'x'} = \sigma_{xx}\cos^2\theta_y \qquad \sigma_{y'y'} = \sigma_{yy} \qquad \tau_{x'y'} = \tau_{xy}\cos\theta_y \tag{d}$$

Combining Eqs. (*b*) to (*d*) yields

$$N_{\theta y} = \frac{h}{f_\sigma \cos \theta_y} \sqrt{(\sigma_{xx} \cos^2 \theta_y - \sigma_{yy})^2 + 4\tau_{xy}^2 \cos^2 \theta_y} \tag{e}$$

In a similar manner it can be shown that the oblique-incidence pattern associated with a rotation about Ox yields

$$N_{\theta x} = \frac{h}{f_\sigma \cos \theta_x} \sqrt{(\sigma_{xx} - \sigma_{yy} \cos^2 \theta_x)^2 + 4\tau_{xy}^2 \cos^2 \theta_x} \tag{f}$$

If the rotation is controlled so that $\theta_x = \theta_y = \theta$, Eqs. (*a*), (*e*), and (*f*) reduce to

$$\begin{aligned}
\frac{N_0^2 f_\sigma^2}{h^2} &= \sigma_{xx}^2 - 2\sigma_{xx}\sigma_{yy} + \sigma_{yy}^2 + 4\tau_{xy}^2 \\
\frac{N_{\theta_y}^2 \cos^2 \theta f_\sigma^2}{h^2} &= \sigma_{xx}^2 \cos^4 \theta - 2\sigma_{xx}\sigma_{yy} \cos^2 \theta + \sigma_{yy}^2 + 4\tau_{xy}^2 \cos^2 \theta \\
\frac{N_{\theta_x}^2 \cos^2 \theta f_\sigma^2}{h^2} &= \sigma_{xx}^2 - 2\sigma_{xx}\sigma_{yy} \cos^2 \theta + \sigma_{yy}^2 \cos^4 \theta + 4\tau_{xy}^2 \cos^2 \theta
\end{aligned} \tag{g}$$

Solving these equations for σ_{xx} or σ_{yy} yields

$$\begin{aligned}
\left(\frac{\sigma_{xx} h}{f_\sigma}\right)^2 &= \frac{\cot^2 \theta}{1 - \cos^4 \theta} [N_{\theta_x}^2 + N_{\theta_y}^2 \cos^2 \theta - N_0^2(1 + \cos^2 \theta)] \\
\left(\frac{\sigma_{yy} h}{f_\sigma}\right)^2 &= \frac{\cot^2 \theta}{1 - \cos^4 \theta} [N_{\theta_y}^2 + N_{\theta_x}^2 \cos^2 \theta - N_0^2(1 + \cos^2 \theta)]
\end{aligned} \tag{14.31}$$

Solutions of Eqs. (14.31) for σ_{xx} and σ_{yy} are sufficient to permit separation of the principal stresses. Addition of σ_{xx} and σ_{yy} gives the value of the first invariant of stress $I_1 = \sigma_1 + \sigma_2$. All other quantities associated with this two-dimensional state of stress can be obtained from the known quantities $\sigma_1 - \sigma_2$, $\sigma_1 + \sigma_2$, σ_{xx}, and σ_{yy} by employing the relations presented in Secs. 1.5 to 1.7.

14.7 SCALING MODEL-TO-PROTOTYPE STRESSES [22–25]

In the analysis of a photoelastic model fabricated from a polymeric material, the question of the applicability of the results is often raised since the prototype is usually a metallic material. Obviously, the elastic constants of the photoelastic model are greatly different from those of the metallic prototype. However, the stress distribution obtained for a plane-stress or plane-strain problem by a photoelastic analysis is usually independent of the elastic constants, and the results can be applied to a prototype constructed from any material. This statement can be established most readily by reference to the stress equation of compatibility for the plane-stress case. Thus by Eqs. (3.15) and (3.17*c*) it is clear that

$$\nabla^2(\sigma_{xx} + \sigma_{yy}) = -(\nu + 1)\left(\frac{\partial F_x}{\partial x} + \frac{\partial F_y}{\partial y}\right) \tag{14.32}$$

This stress equation of compatibility is independent of the modulus of elasticity E and thus shows that the value of the model modulus does not influence the stress distribution. The influence of the other elastic constant ν (Poisson's ratio) depends on the nature of the body-force distribution. If $\partial F_x/\partial x + \partial F_y/\partial y = 0$, the stress distribution is independent of Poisson's ratio. This statement implies that there will be no influence due to Poisson's ratio when

1. $F_x = F_y = 0$ (the absence of body forces)
2. $F_x = C_1$, $F_y = C_2$ (the uniform body-force field, i.e., gravitational)
3. $F_x = C_1 x$, $F_y = -C_1 y$ (a linear body-force field in x and y)

There are two exceptions to this general law of similarity of stress distributions in two-dimensional parts. First, if the two-dimensional photoelastic model is multiply connected, Eq. (14.32) does not apply. In this case the multiply connected body has a hole or series of holes, and the influence of Poisson's ratio will depend upon the nature of the loading on the boundary of the hole. If the resultant force acting on the boundary of the hole is zero, the stress distribution will again be independent of Poisson's ratio. However, if the resultant force applied to the boundary of the hole is not zero, the value of Poisson's ratio will influence the distribution of the stresses. Fortunately, in specific examples of this type where the effect of Poisson's ratio has been evaluated, its influence on the maximum principal stress is usually less than about 7 percent.

The second exception to the laws of similitude is the case where the photoelastic model undergoes appreciable distortion under the action of the applied load. Local distortions are a source of error in notches, for example, since curvatures are modified and the stress-concentration factors are decreased. These model distortions can be minimized by selecting a model material with a high figure of merit and reducing the applied load to the lowest value consistent with adequate model response.

Since the photoelastic model may differ from the prototype in respect to scale, thickness, and applied load, as well as the elastic constants, it is necessary to extend this treatment to include the scaling relationships. A great deal has been written concerning scaling relationships employing dimensionless ratios and the Buckingham π theory; however, in most photoelastic applications, scaling the stresses from the model to the prototype is a relatively simple matter where the pertinent dimensionless ratios can be written directly. For instance, in the case of a two-dimensional model with applied loads P, the dimensionless ratio for stresses is $\sigma hl/P$ and for displacements $\delta Eh/P$. Thus the prototype stresses can be written as

$$\sigma_p = \sigma_m \frac{P_p}{P_m} \frac{h_m}{h_p} \frac{l_m}{l_p} \tag{14.33}$$

and the prototype displacements as

$$\delta_p = \delta_m \frac{P_p}{P_m} \frac{E_m}{E_p} \frac{h_m}{h_p} \tag{14.34}$$

where σ = stress at given point
δ = displacement at given point
P = applied load
h = thickness
l = typical length dimension
and subscripts p and m refer to the prototype and the model, respectively.

In conclusion, it is clear that scaling between model and prototype can be accomplished in most two-dimensional problems encountered by the photoelastician. The modulus of elasticity is never a consideration in determining the stress distribution unless the loading is such that model deformations change the load distribution, e.g., contact stresses. Also, Poisson's ratio need not be considered when the body is simply connected and the body-force field is either absent or uniform, i.e., dead-weight loading.

14.8 MATERIALS FOR TWO-DIMENSIONAL PHOTOELASTICITY

One of the most important factors in a photoelastic analysis is the selection of the proper material for the photoelastic model. Unfortunately, a perfectly ideal photoelastic material does not exist, and the investigator must select from the list of available materials the one which most closely fits his needs. The quantity of photoelastic plastic used each year is not sufficient to entice a chemical company into the development and subsequent production of a polymeric material especially designed for photoelastic applications. As a consequence, the photoelastician must select a model material which is commerically available for some purpose other than photoelasticity.

The following list gives properties which an ideal photoelastic material should exhibit. These criteria are discussed individually below.

1. The material must be transparent to the light employed in the polariscope.
2. The material should be quite sensitive to either stress or strain, as indicated by a low material fringe value in terms of either stress f_σ or strain f_ϵ.
3. The material should exhibit linear characteristics with respect to
   a. Stress-strain properties
   b. Stress–fringe-order properties
   c. Strain–fringe-order properties
4. The material should have both mechanical and optical isotropy and homogeneity.
5. The material should not exhibit time-dependent properties such as creep.
6. The material should exhibit a high modulus of elasticity and a high proportional limit.
7. The material sensitivity, that is, f_σ or f_ϵ, should not change markedly with small variations in temperature.
8. The material should not exhibit time-edge effects.

9. The material should be capable of being machined by conventional means.
10. The material should be free of residual stresses.
11. The material should not be prohibitively expensive.

A. Transparency

In almost all normal applications the materials selected for photoelastic models are transparent plastics. These plastics must be transparent to visible light, but they need not be crystal clear. This transparency requirement is not difficult to meet since most polymeric materials are colored or made opaque by the addition of fillers. The raw materials in the basic polymer, although not crystal clear, are usually transparent.

In certain special applications which require a study of the stresses in normally opaque materials, e.g., germanium or silicon, an infrared polariscope has been used. A few materials are transparent in either the ultraviolet region or the infrared region of the radiant-energy spectrum. Polariscopes can be constructed to operate in either of these regions if advantages can be gained by employing light with very short or very long wavelengths. However, for stress-analysis purposes the visible-light polariscopes are quite adequate.

B. Sensitivity

A highly sensitive photoelastic material is often desirable since it increases the number of fringes which can be observed in the model. If the value of f_σ for a model material is low, a satisfactory fringe pattern can be achieved in the model with relatively low loads. This feature reduces the complexity of the loading fixture and limits the distortion of the model. In the case of birefringent coatings, which will be discussed later, a material with a low value of f_ϵ is essential to reduce errors introduced by the coating thicknesses.

Photoelastic materials are available with values of f_σ which range from less than 0.2 to over 2000 lb/in (0.035 to 350 kN/m). The situation regarding values of f_ϵ is not so satisfactory since materials with a sufficiently low value of f_ϵ are not yet available (f_ϵ usually ranges between 0.0002 and 0.02 in or from 0.005 to 0.50 mm). A material with a value of $f_\epsilon = 0.00002$ in (0.0005 mm) would greatly enhance the applicability of the birefringent coating method of photoelasticity.

C. Linearity

Photoelastic models are normally employed to predict the stresses which occur in a metallic prototype. Since model-to-prototype scaling must be used to establish prototype stresses, the model material must exhibit linear stress-strain, optical-stress, and optical-strain properties. Very few data are available in the open literature on optical-strain relationships; however, since the photoelastic method is usually employed to determine stress differences, this lack of data on strain behavior is not considered serious. Typical stress-strain curves and stress–fringe-order

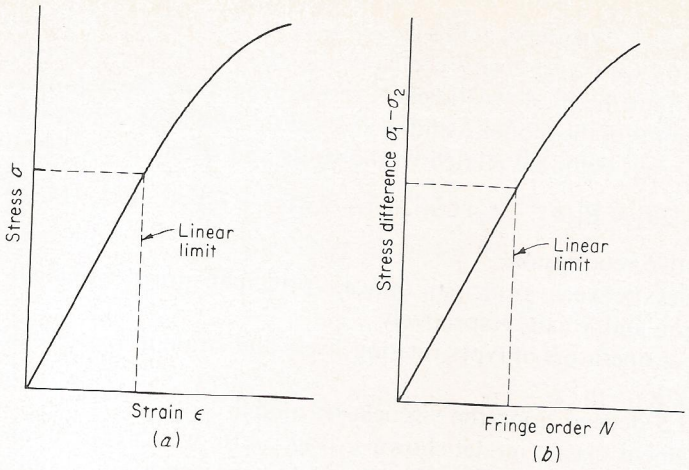

Figure 14.15 Typical (*a*) stress-strain and (*b*) stress-optical response curves for a polymeric photoelastic material.

curves are presented in Fig. 14.15 to show the characteristic behavior of polymeric photoelastic materials. Most polymeric materials exhibit linear stress-strain and stress–fringe-order curves for the initial portion of the curve. However, at higher levels of stress the material may exhibit nonlinear effects. For this reason the higher stress levels are to be avoided in photoelastic tests associated with these nonlinear materials.

D. Isotropy and Homogeneity

Most photoelastic materials are prepared from liquid polymers by casting between two glass plates which form the mold. When the photoelastic materials are prepared by a casting process, the molecular chains of the polymer are randomly oriented and the materials are essentially isotropic and homogeneous. However, certain plastics are rolled or stretched during the production process. In both of these production processes the molecular chains are oriented in the direction of rolling or stretching. These materials will exhibit anisotropic properties (both mechanical and optical) and should therefore be avoided in any photoelastic application except those where anisotropic material properties are required.

E. Creep

Unfortunately, most photoelastic materials of a polymeric base creep both mechanically and optically over the time associated with a photoelastic analysis. Because of the effects of mechanical and optical creep, polymeric materials cannot be truly characterized as elastic materials but must be considered viscoelastic.

One of the first attempts to formulate a mathematical theory of photoviscoelasticity was made by Mindlin [26] by considering a generalized viscoelastic

model consisting of m elastic elements with a shear modulus G_k ($k = 1, 2, 3, \ldots, m$) and m viscous elements with a viscosity coefficient η_k ($k = 1, 2, 3, \ldots, m$) (see Fig. 14.16). Assuming that the photoelastic effect results from only the deformation of the elastic elements of the model, Mindlin showed that the relative retardation, expressed as $n_1 - n_2$, could be related to the stress and strain as

$$(n_1 - n_2) \cos 2\theta_n = R[(\sigma_1 - \sigma_2) \cos 2\theta_\sigma] + 2S[(\epsilon_1 - \epsilon_2) \cos 2\theta_\epsilon] \quad (14.35)$$

where $n_1 - n_2$ = relative retardation

$\theta_n, \theta_\sigma, \theta_\epsilon$ = angles between principal optical, principal stress, principal strain, and x axis, respectively

R, S = linear operators of types relating stress and strain in viscoelastic theory

The operators R and S depend upon the viscoelastic model.

For the three-element elastic model shown in Fig. 14.16, which exhibits instantaneous and delayed elasticity but no flow ($\eta_3 = \infty$), the operators R and S can be expressed as

$$R = \frac{n_0^3}{4G_1}(c_1 - c_2) \qquad S = \frac{n_0^3}{2} c_2 \quad (14.36)$$

These equations show that the birefringence is due to both stress and strain but is independent of stress rate and strain rate. Coker and Filon [3, p. 272] have found that the material xylonite follows this particular viscoelastic model.

It is evident from these results that the optical response exhibited by a photoelastic model depends upon the viscoelastic properties of the model material. In

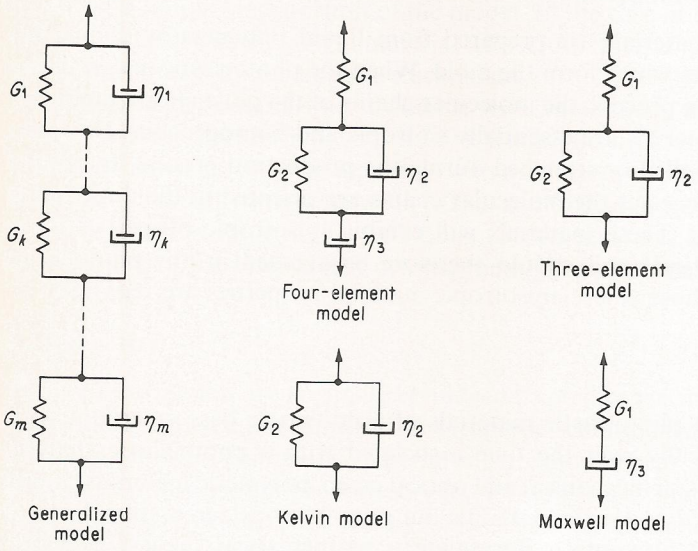

Figure 14.16 Generalized model and elementary viscoelastic models.

the most general case, the retardation can be a function of stress, strain, strain rate, and stress rate. Fortunately, most of the polymers used in photoelasticity are linearly viscoelastic. With linearly viscoelastic materials, the stress and strain, which vary with both position and time, can be represented by the product of two functions: one in space coordinates only and the other in a time coordinate only:

$$\sigma^*(x, y, t) = \sigma(x, y)f(t) \qquad \epsilon^*(x, y, t) = \epsilon(x, y)g(t) \tag{14.37}$$

When Eqs. (14.37) hold, it can be shown that

$$\theta_n = \theta_\sigma = \theta_\epsilon \qquad n_2 - n_1 = C(t)(\sigma_1 - \sigma_2) \qquad n_2 - n_1 = c(t)(\epsilon_1 - \epsilon_2) \tag{14.38}$$

where $$C(t) = R[f(t)] + \frac{1}{G_0} S[g(t)] \qquad c(t) = G_0 R[f(t)] + S[g(t)]$$

and $$G_0 = \frac{\sigma_1 - \sigma_2}{2(\epsilon_1 - \epsilon_2)}$$

This series of equations implies that Eqs. (13.8) and (13.12) can be rewritten in the following forms:

$$\sigma_1 - \sigma_2 = \frac{N}{h} f_\sigma(t) \qquad \epsilon_1 - \epsilon_2 = \frac{N}{h} f_\epsilon(t) \tag{14.39}$$

where f_σ and f_ϵ are written as functions of time rather than as constants.

The results of Eqs. (14.39) are significant since they show that viscoelastic model materials can be employed to perform elastic-stress analyses. Because of the viscoelastic nature of the model materials, the stress and strain material fringe values are functions of time; however, over the short time intervals needed to photograph a fringe pattern they can be considered as constants. A typical plot of the variation in material fringe value with time is shown in Fig. 14.17. For most

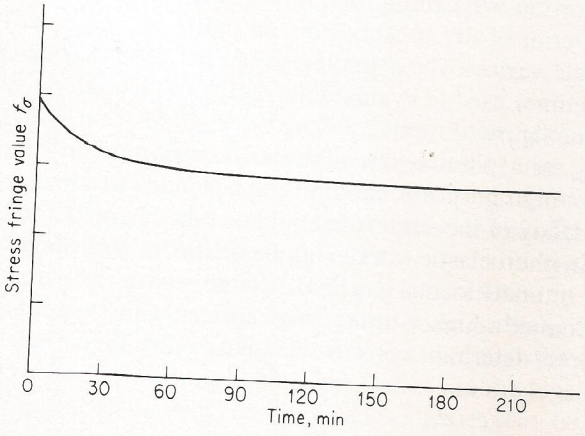

Figure 14.17 Typical curve showing the time-after-loading dependence of the stress fringe value in a viscoelastic polymeric material.

model materials, the stress fringe value f_σ decreases rapidly with time immediately after loading but then tends to stabilize after about 1 h. In practice, the load is maintained on the model until a stable fringe pattern is achieved. The pattern is then photographed, and the stable material fringe value associated with the time of the photograph is used for the analysis. It should be noted that photoelastic materials vary from supplier to supplier and from batch to batch; hence, each sheet of material must be calibrated at the time of the photoelastic analysis to determine $f_\sigma(t)$. Also, in certain photoelastic materials, the polymerization process continues, and f_σ changes with time on a scale of months. Hence, a piece of material stored for a year will, in general, exhibit a higher value of f_σ than the fresh material.

F. Modulus of Elasticity and Proportional Limit

The modulus of elasticity is important in the selection of a photoelastic material because the modulus controls the distortion of the model due to the applied stresses. If a model distorts appreciably, the geometry of its boundary will change and the photoelastic solution is no longer accurate. Errors of considerable magnitude are produced by model distortion, where small changes in the boundary contour are influential in determining the stress distribution. For example, a strip with a very sharp notch theoretically will have a very high stress concentration at the root of the notch. If the model distorts under load, the sharpness of the notch is decreased and the experimentally determined stress concentration is reduced. Another case which exists where model distortion influences the photoelastically determined results is the contact problem. In this instance the stress distribution is a function of the penetration and bearing area of the loading point. Obviously, the modulus of elasticity is influential in controlling both of these quantities.

The factor which can be used to judge the various photoelastic materials in regard to their ability to resist distortion is $1/f_\epsilon$ or $E/f_\sigma(1 + \nu)$. The best photoelastic materials to resist distortion will exhibit high values of $1/f_\epsilon$ or low values for the material fringe value in terms of strain. Since Poisson's ratio for most rigid polymeric photoelastic materials varies over a limited range between 0.36 and 0.42, the ratio $Q = E/f_\sigma$ is sometimes used to evaluate the merits of the materials. This factor E/f_σ is known as the figure of merit.

The proportional limit σ_{pl} of a photoelastic material is important in two respects. First, a material with a high proportional limit can be loaded to a higher level without endangering the safety of the model (it should be noted here that the polymers normally employed in photoelastic work exhibit a brittle fracture and as such fail disastrously when the ultimate load is reached). Second, a material with a high proportional limit can produce a higher-order fringe pattern which tends to improve the accuracy of the stress determinations. A sensitivity index for a model material can be defined as

$$S = \frac{\sigma_{pl}}{f_\sigma} \tag{14.40}$$

Superior model materials exhibit high values for both the sensitivity index S and the figure of merit Q.

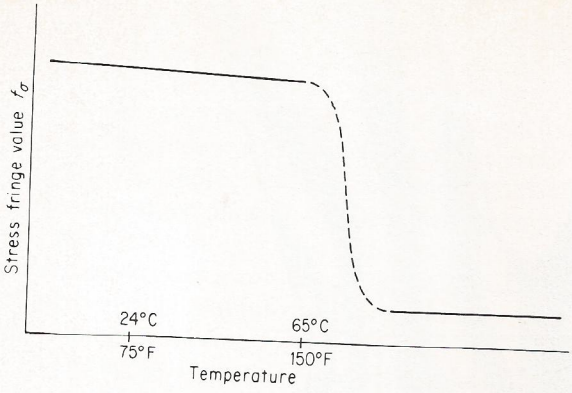

Figure 14.18 Typical curve showing the change in stress fringe value with temperature.

G. Temperature Sensitivity [27]

If the material fringe value in terms of stress changes markedly with temperature, errors can be introduced in a photoelastic analysis by minor temperature variations during the period involved in obtaining a photoelastic pattern. A typical curve showing the general characteristics of the change in material fringe value with temperature is shown in Fig. 14.18. For most polymeric plastics there is a linear region of this curve where f_σ decreases slightly with temperature. For one commonly used epoxy, the change in f_σ is only 0.07 lb/(in)(°F) [0.022 kN/(m)(°C)] in this linear region. However, at temperatures in excess of 150°F (65°C), the value of f_σ begins to drop sharply with increase in temperature, as shown in Fig. 14.18. For conventional two-dimensional photoelastic studies conducted at room temperature (75°F or 24°C), the slope of the curve in the linear region is the important characteristic. For most of the commonly used materials the slope is modest in this region, so that variations in f_σ can be neglected if temperature variations are limited to the range of ± 5°F (± 3°C).

H. Time-Edge Effect [28, 29]

When a photoelastic model is machined from a sheet of plastic and examined under a no-load condition as a function of time, it is noted that a stress is induced on the boundary which produces a fringe or a series of fringes that parallel the boundary of the model. An example of a model with a severe case of time-edge effect is illustrated in Fig. 14.19.

The influence of these time-edge effects on a photoelastic analysis is quite important. The fringe pattern observed is due to the superposition of two states of stress, the first associated with the load and the second a result of the time-edge stresses. Since the time-edge stresses are the most predominant on the boundary, the errors introduced by the edge stresses may be quite large in the determination of the extremely important boundary stresses.

It has been established that the time-edge effect is caused by diffusion of water vapor from the air into the plastic or from the plastic into the air.

For many photoelastic plastics, the diffusion process is so slow at room

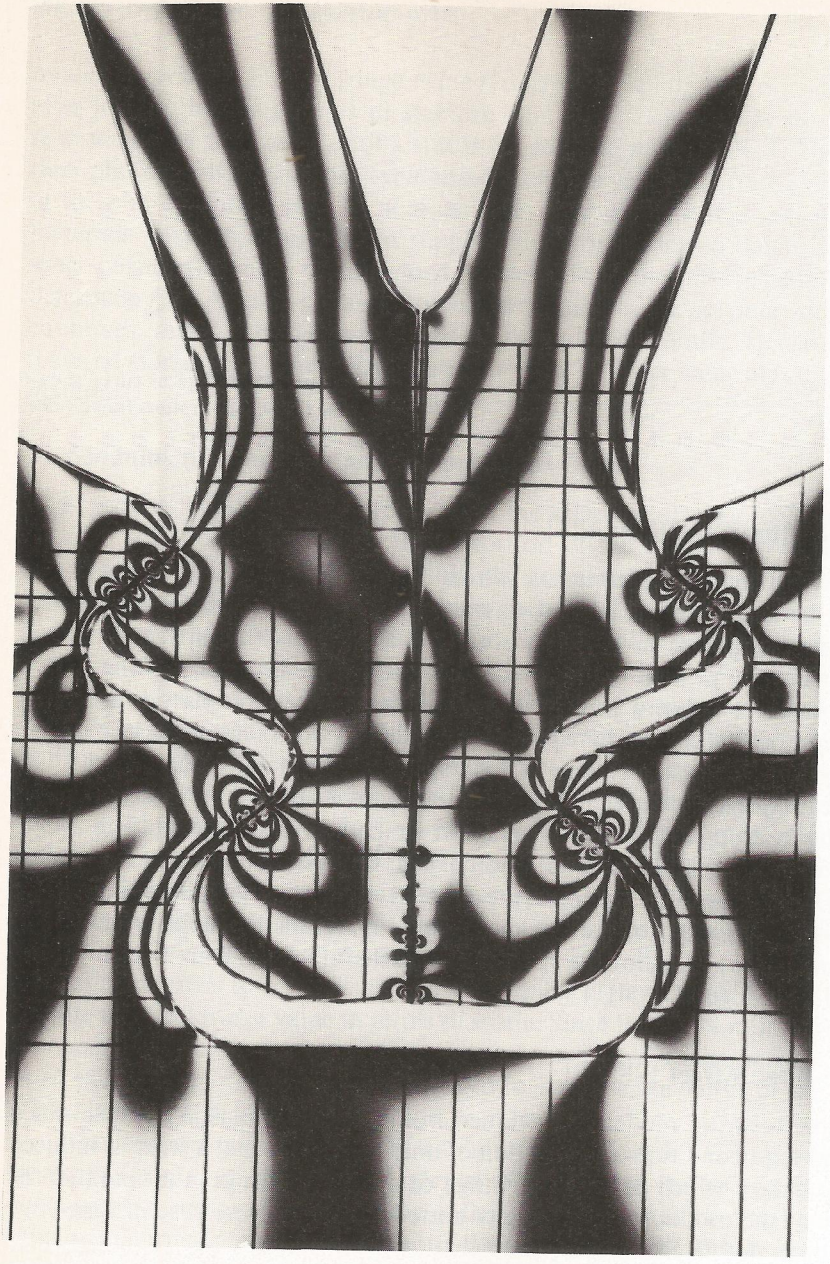

Figure 14.19 Time-edge stresses in a photoelastic model of a turbine-blade dovetail joint (note the distortion of the fringe pattern near the boundary due to time-edge stresses).

temperature that it requires many years to reach an equilibrium state. For this reason, a freshly machined edge of a model usually will be in a condition to accept water from the air (its central region has not been saturated), and time-edge stresses will begin to develop. The rate at which the time-edge stresses develop for a particular model will depend upon the relative humidity of the air and the temperature. Photoelastic tests conducted at relative humidities of greater than 80 percent are often difficult, for the time-edge stresses become objectionably large in less than 2 to 3 h. For most photoelastic plastics the proper procedure to avoid time-edge stresses is to select relatively dry days (relative humidity less than 40 to 50 percent) and to photograph the model as soon as possible after completing the machining process.

The epoxy resins are somewhat different from most other photoelastic materials in that their diffusion rate is sufficiently high that a saturated condition can be established after about 2 to 3 months. If a two-dimensional model is machined from a sheet of material that has been maintained at a constant humidity for several months so that it is in a state of equilibrium (concentration uniform through the thickness of the sheet), and if the model is tested under these same humidity conditions, time-edge stresses will not develop.

I. Machinability

Photoelastic materials must be machinable in order to form the complex models employed in photoelastic analyses. Ideally, it should be possible to turn, mill, route, drill, and grind these plastics. Although machinability properties may appear to be a trivial requirement, it is often extremely difficult to machine a high-quality photoelastic model properly. The action of a cutting tool on the plastic often produces heat coupled with relatively high cutting forces. As a consequence, boundary stresses due to machining can be introduced permanently into the model, making it unsuitable for a quantitative photoelastic analysis.

In machining photoelastic models, care must be taken to avoid high cutting forces and the generation of excessive amounts of heat. These requirements can best be accomplished by using sharp carbide-tipped tools, air cooling, and light cuts coupled with a relatively high cutting speed. For two-dimensional applications, complex models may be routed from almost any thermosetting plastic. In this machining method a router motor (20,000 to 40,000 r/min) is used to drive a carbide rotary file. The photoelastic model is mounted to a metal template which describes the exact shape of the final model. The plastic is rough-cut with a jigsaw to within about $\frac{1}{8}$ in (3 mm) of the template boundary. The final machining operation is accomplished with the router, as illustrated in Fig. 14.20. The metal template is guided by an oversize-diameter pin which is coaxial with the rotary file. The rate of feed along the boundary of the model is carefully controlled by moving the model along the pin by hand. Successive cuts are taken by reducing the diameter of the stationary pin until it finally coincides with the cutter diameter. By using this technique, satisfactory two-dimensional models can be produced in less than 1 h by skilled operators.

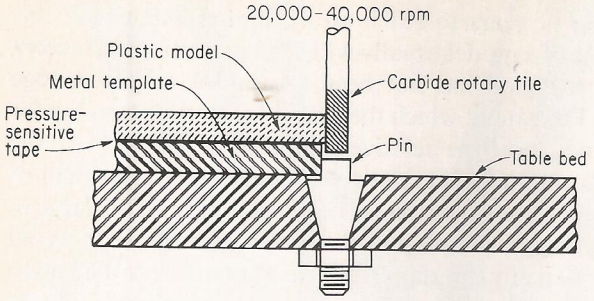

Figure 14.20 Machining a two-dimensional photoelastic model with a router.

J. Residual Stresses

Residual stresses are sometimes introduced into photoelastic plastics during casting and curing operations and almost always by rolling or extrusion processes. They can be observed simply by inserting the sheet of material in a polariscope and noting the order of the fringes in the sheet. The presence of residual stresses in photoelastic models is extremely detrimental since they are superimposed on the true stress distribution produced by loading the model. Since it is difficult if not impossible to subtract out the contribution due to the residual-stress distribution, the presence of residual stresses in the model material often introduces serious errors into a photoelastic analysis.

In certain cases it is possible to reduce the level of the residual stresses by thermally cycling the sheet above its softening point on a flat plate or in an oil bath. However, it is almost impossible to remove all residual stresses completely from a sheet of material once they have been introduced by the manufacturing process. Often it is more expeditious for the photoelastician to cast his own resin into plates, paying particular attention to the curing cycle and mold-release agent, than to purchase materials which must be stress-relieved.

K. Cost of Material

Normally the cost of the model material in a photoelastic analysis represents a very small percentage of the total cost of the investigation. For this reason, the cost of the materials should not be overemphasized, and the most suitable material should be selected on the basis of other parameters, regardless of the apparent difference in cost of the material on a pound basis. Very few two-dimensional photoelastic models require more than 1 or 2 lb of sheet plastic; therefore, prices of $20 to $40 per pound should be considered reasonable if the surface finish is adequate and the sheet is free of residual stress.

14.9 PROPERTIES OF COMMONLY EMPLOYED PHOTOELASTIC MATERIALS [30–39]

A brief examination of the photoelastic literature will show that most polymeric materials exhibit temporary double refraction and that numerous materials have been employed in photoelastic analyses. The list will include several types of glass,

celluloid, gelatin, the glyptal resins, natural and synthetic rubber, fused silica, the phenolformaldehydes, polycarbonate, allyl diglycol (CR-39), and several compositions of the epoxies and the polyesters. Today, most elastic-stress analyses are conducted by employing one of the following materials:

1. Columbia resin CR-39
2. Homalite 100
3. Polycarbonate
4. Epoxy resin
5. Urethane rubber

A. Columbia Resin CR-39 [30, 31]

CR-39 is an allyl diglycol carbonate which is produced by reacting phosgene with diethylene glycol to obtain a chloroformate, which is then esterified with allyl alcohol to yield a monomer. The monomer is polymerized by heating in the presence of a catalyst (benzoyl peroxide), and the resultant sheet is a crystal-clear product. The casting operation is performed in such a manner that the final product in sheet form has surfaces of optical quality. Actually this is the predominant advantage of CR-39, namely, that it is available in large sheets 48 by 60 in (1.2 by 1.5 m) of a number of different thicknesses with a surface finish which is nearly optically perfect. The material is quite brittle and is difficult to turn or to mill; however, it can be readily machined by routing, and a high-quality photoelastic model can usually be produced in less than 1 h.

The material has a relatively low fringe value, indicating sensitivity, but its sensitivity index S is impaired by the low stress value at which it becomes nonlinear. CR-39 exhibits appreciable creep; therefore, the material fringe value must be determined as a function of time. The material is less prone to time-edge effects than the epoxies but more susceptible to time-edge effect than the polyesters (Homalite 100) or polycarbonate.

B. Homalite 100

Homalite 100 is a polyester resin which is cast between two plates of glass to form very large sheets. The surfaces of the commercially available sheets are of optical quality, and the material is free of residual stresses. Models can be machined by routing; however, since the material is extremely brittle, edge chipping can be a problem.

Homalite 100 does not exhibit appreciable creep; therefore, the material fringe value can be treated as a constant for loading times in excess of 5 to 10 min. Since moisture absorption is very slow in this material, time-edge effects do not become apparent for several days even under very humid test conditions. The material exhibits both a low figure of merit Q and a low sensitivity index S. High fringe orders cannot be achieved without fracturing the model.

C. Polycarbonate

Polycarbonate is an unusually tough and ductile polymer which yields and flows prior to fracture. It is known by the trade name Lexan in the United States and as Makrolan in Europe. Polycarbonate exhibits both a high figure of merit Q and a high sensitivity index S. It is relatively free of time-edge effects and exhibits very little creep at room temperature.

Polycarbonate is a thermoplastic and is produced in sheet form by an extrusion process. It is available in large sheets with reasonably good surface characteristics. Unfortunately, the extrusion process usually produces some residual birefringence in the sheets. Annealing for an extended period of time at or near the softening temperature is required to eliminate the residual birefringence. The polycarbonate material is also difficult to machine. Any significant heat produced by the cutting tool will cause the material to soften and deform under the tool. Routing can be performed only under water, and side milling is practically impossible. Band sawing and hand filing are often required to produce satisfactory model boundaries. Since the material exhibits both yield and flow characteristics, it can also be employed for photoplastic studies. The birefringence introduced in the plastic state is permanent and is locked into the material on a molecular scale. This behavior makes the material suitable for three-dimensional photoplasticity studies.

D. Epoxy Resin [32]

Epoxy resins were first introduced in photoelastic applications in the mid-1950s, when they were employed predominantly as materials for three-dimensional photoelasticity. However, a brief review of their properties indicates that they are also quite suitable for use in a wide variety of two-dimensional applications. The commercial epoxy resins are condensation products of epichlorohydrin and a polyhydric phenol. The basic monomer can be polymerized by using acid anhydrides, polyamides, or polyamines. In general, curing with the acid anhydrides requires higher temperatures than curing with the polyamides or polyamines.

A wide variety of epoxy materials can be cast into sheet form. The type of the basic monomer, the curing agent, and the percentage of the curing agent relative to the basic monomer can be varied to give an almost infinite number of epoxy materials. One particular epoxy, ERL-2774 with 50 parts per hundred by weight of phthalic anhydride, is a material which can be readily adapted for photoelastic work. This epoxy can be cast into sheets which are light amber in appearance; however, optical-quality surfaces are difficult to produce, and surface finishing by fly cutting or milling is frequently required. The epoxies are usually characterized as brittle materials, but they are easier to machine than the polyesters or CR-39. Most of the epoxies exhibit better optical sensitivity than Homolite 100 or CR-39; they are less sensitive than polycarbonate.

Although the material is susceptible to time-edge effects, the rate of diffusion of water into epoxy is sufficiently high to permit a saturation condition to be

achieved in about 2 months. If the sheets are stored until saturated at, say, a 50 percent relative humidity, the model can be cut from the conditioned sheet and little or no time-edge effect will be noted unless the humidity conditions change. Finally, the material creeps approximately the same amount as polycarbonate or Homolite 100 but much less than CR-39.

E. Urethane Rubber [33]

Urethane rubber is an unusual photoelastic material in that it exhibits a very low modulus of elasticity (three orders of magnitude lower than that of the other materials listed) and a very high sensitivity, as indicated by an f_σ value of less than 1 lb/in (0.175 kN/m). The material can be cast between glass plates to produce an amber-colored sheet with optical-quality surfaces. Except for its very low figure of merit, the material ranks relatively well in comparison with the other materials listed. Its strain sensitivity is so low that time-edge effects are negligible; moreover, in spite of its low modulus, the material exhibits little mechanical or optical creep. The material can readily be machined on a high-speed router, but it must be frozen at liquid-nitrogen temperatures before its surfaces can be turned or milled.

The material is particularly suited for demonstration models. Loads applied by hand are sufficient to produce well-defined fringe patterns, and the absence of time-edge effects permits the models to be stored for years. Also, the material is so sensitive to stress that it can be used to study body-force problems if fringe-multiplication techniques are employed with thick models. Finally, urethane rubber can be used for models in dynamic photoelasticity, where its low modulus of elasticity has the effect of lowering the velocity of the stress wave to less than 300 ft/s (90 m/s) as compared with 6000 ft/s (1830 m/s) in CR-39. The low-velocity stress waves in urethane-rubber models are easy to photograph with moderate-speed framing cameras (10,000 frames per second), which are common, while the high-speed stress waves in CR-39 require high-speed cameras (200,000 frames per second or more) to produce satisfactory fringe patterns for analysis.

F. Conclusions Pertaining to Material Selection

A summary of the mechanical and optical properties of the five photoelastic materials is presented in Table 14.2. It is clear by comparing the figure of merit Q and the sensitivity index S that polycarbonate and the epoxies exhibit superior properties. Unfortunately, the polycarbonate material is difficult to machine, and the epoxy resin materials require special precautions to minimize time-edge effects.

Homalite 100 and CR-39 can be used in applications where high precision and low model distortion are not required. Both have the advantage of being available in large sheets with optical-quality surfaces. Homolite 100 is often preferred since it exhibits less creep and exhibits much less time-edge effect than CR-39. The sensitivity index S of CR-39, however, is significantly less than that of Homalite 100.

Table 14.2 Summary of the optical and mechanical properties of several photoelastic materials

Property	CR-39	Homalite 100	Polycarbonate	Epoxy resin ERL-2774 †	Epoxy resin ERL-2774 ‡	Urethane rubber§
Time-edge effect	Poor	Excellent	Excellent	Good	Good	Excellent
Creep	Poor	Excellent	Excellent	Good	Good	Excellent
Machinability	Poor	Good	Poor	Good	Good	Poor
Modulus of elasticity E:						
lb/in^2	250,000	560,000	360,000	475,000	475,000	450
MPa	1725	3860	2480	3275	3275	3
Poisson's ratio ν	0.42	0.35	0.38	0.38	0.36	0.46
Proportional limit σ_{pl}:						
lb/in^2	3000	7000	5000	8000	8000	20
MPa	20.7	48.3	34.5	55.2	55.2	0.14
Stress fringe value f_σ ¶:						
lb/in	88	135	40	58	64	1
kN/m	15.4	23.6	7.0	10.2	11.2	0.18
Strain fringe value f_ϵ ¶:						
in	0.00050	0.00033	0.00015	0.00017	0.00018	0.00324
mm	0.0127	0.0084	0.0038	0.0043	0.0046	0.082
Figure of merit Q:						
1/in	2840	4150	9000	8200	7400	450
1/mm	112	163	354	321	292	17
Sensitivity index S:						
1/in	34	52	125	138	125	20
1/mm	1.34	2.05	4.92	5.43	4.92	0.78

† With 50 parts per hundred phthalic anhydride.

‡ With 42 parts per hundred phthalic anhydride and 20 parts per hundred hexahydrophthalic anhydride.

§ 100 parts by weight Hysol 2085 with 24 parts by weight Hysol 3562.

¶ For green light ($\lambda = 546.1$ nm).

Urethane rubber is extremely useful in special-purpose applications such as demonstration models for instructional purposes. Because of its low material stress fringe value it is also useful for modeling where body forces due to gravity produce the loads. Finally, urethane rubber can be used to great advantage in dynamic photoelastic studies, where its low modulus of elasticity results in low-velocity stress waves which are easy to photograph.

EXERCISES

14.1 Plot the fringe orders as a function of position across the horizontal centerline of the chain-link model shown in Fig. 14.1.

14.2 Determine the fringe orders associated with the tensile and compressive stress concentrations at the pinholes of the chain-link shown in Fig. 14.1.